Structural Durability &
Health Monitoring

Tech Science Press

https://doi.org/10.32604/sdhm.2026.079519

ARTICLE

Study on Wind-Induced Vibration Response and CFRP Material Reinforcement of Masonry Structure Pagoda

Jia Wang[1], **Jiayu Zhou**[1], **Kangjie Ling**[1], **Dewen Liu**[1,2,*] **and Chenghao Xu**[3,*]

[1]College of Civil Engineering, Southwest Forestry University, Kunming, China
[2]International College, Krirk University, Bangkok, Thailand
[3]School of Civil Engineering & Architecture, Wenzhou Polytechnic, Wenzhou, China

*Corresponding Authors: Dewen Liu. Email: civil_liudewen@sina.com; Chenghao Xu. Email: 42174961@163.com

Received: 22 January 2026; Accepted: 16 March 2026; Published: 30 June 2026

ABSTRACT: This study investigates the wind-resistant performance of a masonry pagoda using ABAQUS. Modal analysis was first conducted to identify the first six vibration modes. Wind speed time histories generated via the harmonic superposition method in MATLAB were converted into wind pressure and applied to the pagoda's surface. The time-history analysis method was employed to study wind-induced vibrations, obtaining nodal displacement time-history responses. Comparative analyses of structural responses were performed under 0° and 90° wind directions. Finally, Carbon fiber reinforced plastic (CFRP) reinforcement was applied, with post-reinforcement damage analysis systematically compared to the pre-reinforcement damaged state. The results demonstrate that the door openings and damaged areas of the pagoda exhibit heightened wind sensitivity. The structural displacement response primarily occurs along the Z-axis, with magnitudes increasing proportionally to elevation. The 90° wind direction is identified as the most critical, inducing maximum dynamic responses. CFRP reinforcement effectively reduces displacement and stress values while significantly improving structural stability.

KEYWORDS: Ancient masonry pagoda; harmonic superposition method; fluctuating wind; ABAQUS; time history analysis

1 Introduction

Structural wind engineering, foundational to the discipline's development, remains central to wind engineering research, with mitigating wind-induced disasters constituting a critical mission for human survival and development. Consequently, research on structural wind engineering holds critical significance. Substantial advancements in computational wind engineering have been achieved through extensive scholarly efforts [1–3]. Chinese ancient architecture, characterized by its millennia-old history, aesthetic elegance, and unique cultural value, represents architectural treasures of global significance. The conservation of heritage structures has gained increasing attention, evidenced by 280 ancient buildings (36.7%) among 762 sites in the 8th batch of National Key Cultural Relics Protection Units. Current research predominantly focuses on structural strength and seismic performance [4], while wind resistance studies remain limited. Pagoda structures, as wind-sensitive tall constructions, exhibit pronounced vulnerability to lateral loads, frequently experiencing vibration and deformation under wind actions.

Scholars worldwide have conducted preliminary investigations on ancient structures, particularly pagoda configurations, under wind loads. These studies primarily focus on wind load modeling, structural response analysis, and wind resistance performance evaluation of pagodas. For instance, Li et al. [5] investigated wind load effects on a historic wooden pagoda with distinctive architectural profiles through wind tunnel tests, revealing wind pressure distribution patterns under varying wind speeds, thereby providing a scientific reference framework for sustainable heritage conservation. Additionally, Computational Fluid Dynamics (CFD) simulations have been extensively applied to wind load analysis of pagodas. For example, Li et al. [6] conducted comparative analyses of geometric models with varying levels of detail via CFD simulations, assessed wind effects on ancient Asian wooden pagodas, proposed structural optimization strategies for enhancing wind resistance and structural stability, and established scientific guidelines for conservation and restoration practices.

Research on ancient structures also focuses on structural responses and wind resistance. Wu et al. [7] developed a numerical model of a vase-shaped masonry pagoda using ABAQUS finite element software, analyzing its dynamic responses under seismic waves and revealing principal tensile stress distribution patterns and seismic damage mechanisms. Furthermore, Li et al. [8] proposed a non-destructive approach by planting artificial vegetation around the Yingxian Wooden Pagoda to mitigate wind loads and wind-induced responses. This method centers on creating vegetation barriers to alter flow field characteristics, thereby reducing wind loads acting on the structure, offering an innovative strategy for heritage conservation.

The coupled effects of wind and seismic loads on tall pagodas constitute a key research focus. Tan et al. [9] investigated the vulnerability of seismically isolated high-rise structures under wind actions, establishing a theoretical framework for wind-induced vulnerability assessment validated through case studies. Lu et al. [10] analyzed the dynamic performance and damage patterns of super-tall pagodas under combined seismic and wind loads through field dynamic testing and numerical simulations. Structural optimization strategies have been proposed to enhance wind resistance, including aerodynamic shape optimization of high-rise configurations to mitigate wind load effects as demonstrated by Al-Azri et al. [11]. Han et al. [12] employed CFD simulations and finite element analysis to characterize wind-induced vibration mechanisms in traditional Chinese city gate towers like Nanjing Drum pagoda, providing quantitative foundations for structural retrofitting.

In China, many ancient pagodas have experienced structural damage due to wind loads. A notable example is the Shengxiang Pagoda during the construction of Wuhan Metro Line 5. During tunnel blasting for the metro line, the pagoda exhibited noticeable cracks and displacement due to combined effects of blast-induced vibrations and wind loads. Through numerical simulations and field monitoring, researchers analyzed the dynamic response of the pagoda structure and proposed reinforcement measures, such as carbon fiber reinforced polymer (CFRP) strengthening, to enhance the tower's wind resistance [13].

Current research methods and technologies for building wind loads can be categorized into three approaches: finite element analysis (FEA), computational fluid dynamics (CFD) simulations, and wind tunnel testing.

Finite Element Analysis (FEA) is a widely used method to study structural responses under wind loads. By constructing three-dimensional models, FEA simulates the dynamic effects of wind loads on structures and predicts potential failure modes. For instance, Zhong et al. [14] investigated wind-induced vibrations in transmission line-insulator systems under downburst conditions using static and dynamic FEA methods. Their work established an average wind model and non-stationary fluctuating wind model for downbursts, proposing a method to determine equivalent static wind loads for downburst-affected conductors. Wei et al. [15] comprehensively evaluated and improved the wind resistance of wind turbine towers through FEA, providing theoretical and practical guidance for their design, manufacturing, and optimization. Wang et al. [16] conducted detailed stress, strain, and deformation analyses of wind turbine components via FEA, assessing their load-bearing performance under wind and gravitational loads, thereby offering critical data for turbine design and optimization.

Computational Fluid Dynamics (CFD) Simulations are employed to analyze wind field effects on structures, particularly wind pressure distribution and wind-induced vibration characteristics. This method aids in optimizing structural design to mitigate wind-induced damage. Irwin [17] utilized CFD to study flow characteristics around super-tall buildings in wind fields, revealing detailed flow field patterns to inform architectural design. CFD also enables simulation of building environmental performance (e.g., wind loads, acoustics, optics) for holistic optimization. Janssen et al. [18] applied CFD to simulate wind loads on container ships under varying wind conditions, demonstrating its accuracy in predictions while noting that geometric simplification impacts result reliability.

Wind Tunnel Testing remains a critical experimental method for studying wind load responses. By replicating real-world wind conditions, it provides structural response data across wind speeds to guide reinforcement design. Prasad et al. [19] investigated wind load characteristics of low-rise buildings with varying roof configurations (flat, pitched, etc.) through wind tunnel tests, validating the significant impact of roof design on wind loads and offering scientific guidance for architectural practices. Jiang et al. [20] simulated snowdrift patterns under diverse wind speeds and directions using scaled models in wind tunnels, measuring snow distribution and drift behavior. The resulting data served as a validation benchmark for numerical simulations, ensuring their accuracy and reliability.

This study focuses on a masonry ancient pagoda, examining its academic significance derived from the complexity of wind resistance analysis for its earthquake-damaged unique configuration, as well as its inherent historical value. Wind loads acting on the structure primarily include along-wind mean wind and fluctuating wind components, as well as crosswind wake vortex interference. The residual pagoda in this study is situated in an open terrain with minimal surrounding modern structures, rendering wake vortex effects non-critical. The research specifically addresses structural vibrations induced by along-wind fluctuating wind, neglecting wind-structure interaction effects. Based on national structural design codes, fluctuating wind loads were simulated by accounting for the vertical correlation of wind fluctuations. A three-dimensional finite element model of the pagoda was developed using the simulated time-history samples of fluctuating wind loads, and the wind-induced dynamic responses were calculated through time-history analysis. The structural geometry was modeled using ABAQUS finite element analysis software.

2 The Establishment of the Residual Pagoda Model

2.1 Overview of the Ancient Pagoda

The an Ganyin Temple Pagoda was originally constructed in 1165 CE. Featuring an octagonal plan, the pagoda initially comprised twelve stories with a total height of 44.1 m. In 1303 CE, an earthquake caused the collapse of its upper section, splitting the structure into two parts. Currently, only seven stories remain, with a total residual height of 34.1 m. Due to severe damage to the ancient brick structure, localized geometric simplifications were implemented in numerical modeling. In this study, a three-dimensional numerical model was developed using SolidWorks. The numerical geometry was constructed based on existing architectural records and visual inspection from available photographs, explicitly capturing the macroscopic split between Towers A and B. Minor surface cracks were not modeled as discrete gaps but were homogenized into the material properties to maintain computational efficiency. The pagoda's external and internal side lengths are 4.2 and 1.6 m, respectively, with a current height of 34.1 m. The first story measures 9.98 m in height, while subsequent stories are 14.96, 19.34, 23.44, 27.15, 31.54, and 34.12 m, respectively. The numerical model, alongside field photographs and dimensional schematics, is illustrated in Fig. 1. For clarity, the shorter residual section is designated as Tower A, while the taller portion is referred to as Tower B.

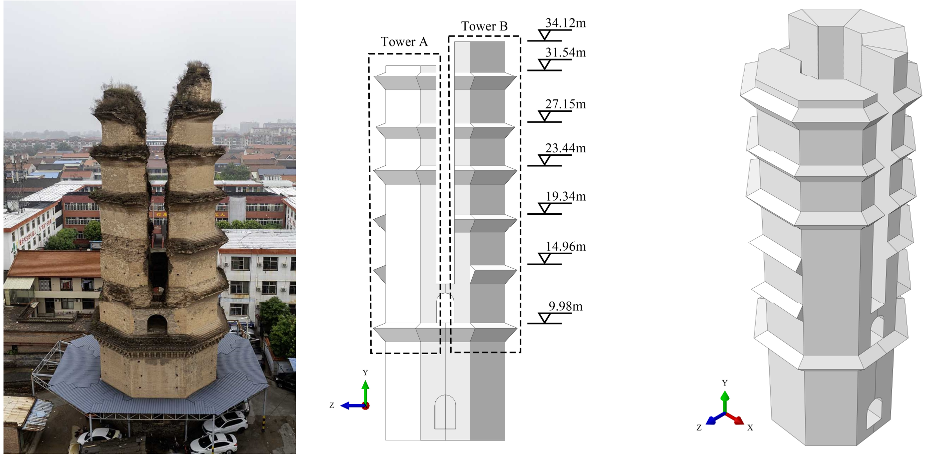

(**a**) Actual scene pictures (**b**) Dimensional schematic (**c**) Three-dimensional numerical model

Figure 1: Ganying temple pagoda.

For the purpose of wind load analysis, a Cartesian coordinate system is defined with the Y-axis vertical (elevation), the Z-axis oriented parallel to the U-shaped opening, and the X-axis perpendicular to the Z-axis (i.e., parallel to the line connecting Towers A and B). This coordinate system is used consistently throughout the study to define wind directions and report displacement responses.

2.2 Finite Element Modeling and Material Characterization

The numerical model was imported into ABAQUS for simulation, with explicit algorithms in the Standard module employed for nonlinear dynamic analysis. The pagoda was discretized using C3D4 tetrahedral elements, selected for their computational efficiency (4-node configuration) and adaptability to complex architectural features (e.g., arches, windows), ensuring geometric fidelity in mesh generation.

The material properties of the masonry were comprehensively determined based on damaged brick testing (Fig. 2) and relevant literature regarding the residual mechanical properties of similar damaged ancient masonry towers [21]. The key material parameters are defined as follows: elastic modulus E = 1250 MPa, density ρ = 1800 kg/m^3, and Poisson's ratio ν = 0.3. A mesh convergence study was performed to ensure the chosen mesh density provides accurate results without being computationally prohibitive. Using C3D4 tetrahedral elements, the global mesh size was progressively refined from 1.0 to 0.8, 0.6, and finally 0.5. At each refinement level, the maximum stress and displacement at critical locations were monitored. When the global mesh size reached 0.5, the computed values differed by less than 2% compared to an even finer mesh (0.4), indicating that the solution had effectively converged. At the same time, this mesh density maintained reasonable computational cost. Based on this study, the global mesh size of 0.5 was selected for all subsequent analyses. Specifically, the selected elastic modulus accurately reflects the tower's actual stiffness state following centuries of environmental erosion, mortar degradation, and localized cracking. Compared to intact historical masonry structures (typically ranging from 2000 to 5000 MPa), this value is significantly lower. In the context of structural safety assessment, adopting a lower elastic modulus embodies a conservative principle: the reduction in structural stiffness leads to an increase in the calculated wind-induced dynamic response. Consequently, this ensures that the conclusions regarding structural safety and the effectiveness of Carbon Fiber Reinforced Polymer (CFRP) reinforcement possess adequate safety margins. Furthermore, given the brittle nature of historical masonry and its concrete-like mechanical characteristics, the Concrete Damaged Plasticity (CDP) model in ABAQUS was adopted to define the constitutive relationship of the masonry. Specifically, while the damage evolution parameters were derived directly from testing, the plasticity parameters (e.g., dilation angle and viscosity) were selected based on established literature values for quasi-brittle materials to ensure numerical stability. The resulting mechanical behavior is illustrated in Fig. 3.

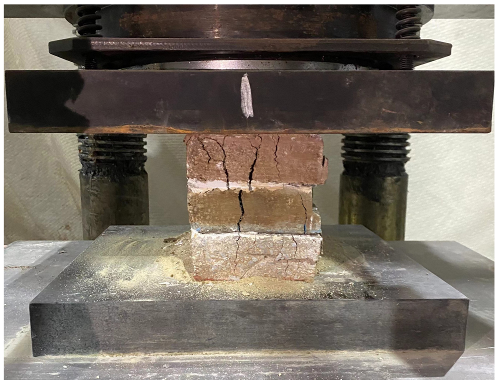

Figure 2: Masonry compression test.

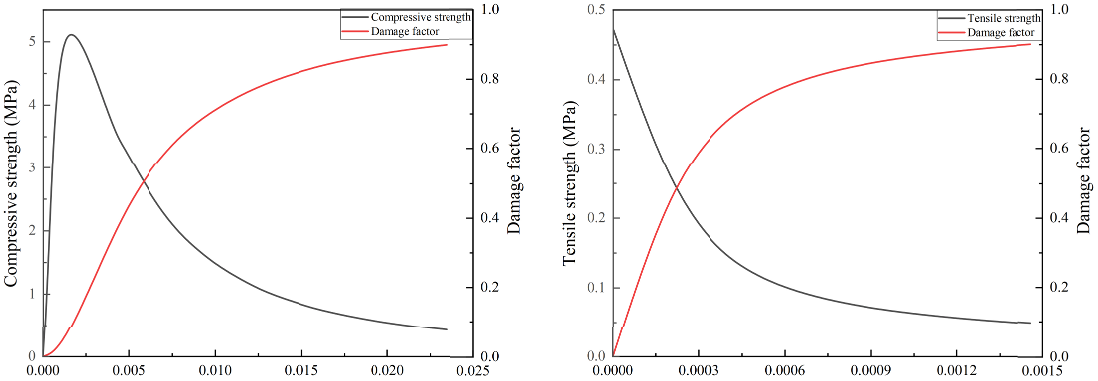

(**a**) Compressive constitutive relationship and damage factor

(**b**) Tensile constitutive relationship and damage factor

Figure 3: Damage factor evolution patterns.

2.3 Modal Analysis

The structural model was developed in ABAQUS to compute the first six vibration modes. Table 1 presents the corresponding natural periods and frequencies of the ABAQUS model.

Table 1: First six natural frequencies and corresponding periods.

Vibration Mode Order	1	2	3	4	5	6
Frequency (Hz)	0.7727	0.9878	1.0748	1.7825	2.9458	3.3997
period (s)	1.2942	1.0124	0.9304	0.5610	0.3395	0.2941

The first six mode shapes of the structure are illustrated in Fig. 4. By extracting the structure's natural vibration characteristics, the complex dynamic response problem is transformed into a linear superposition of individual modal responses through the modal superposition method, enabling efficient computation of wind-induced dynamic behavior.

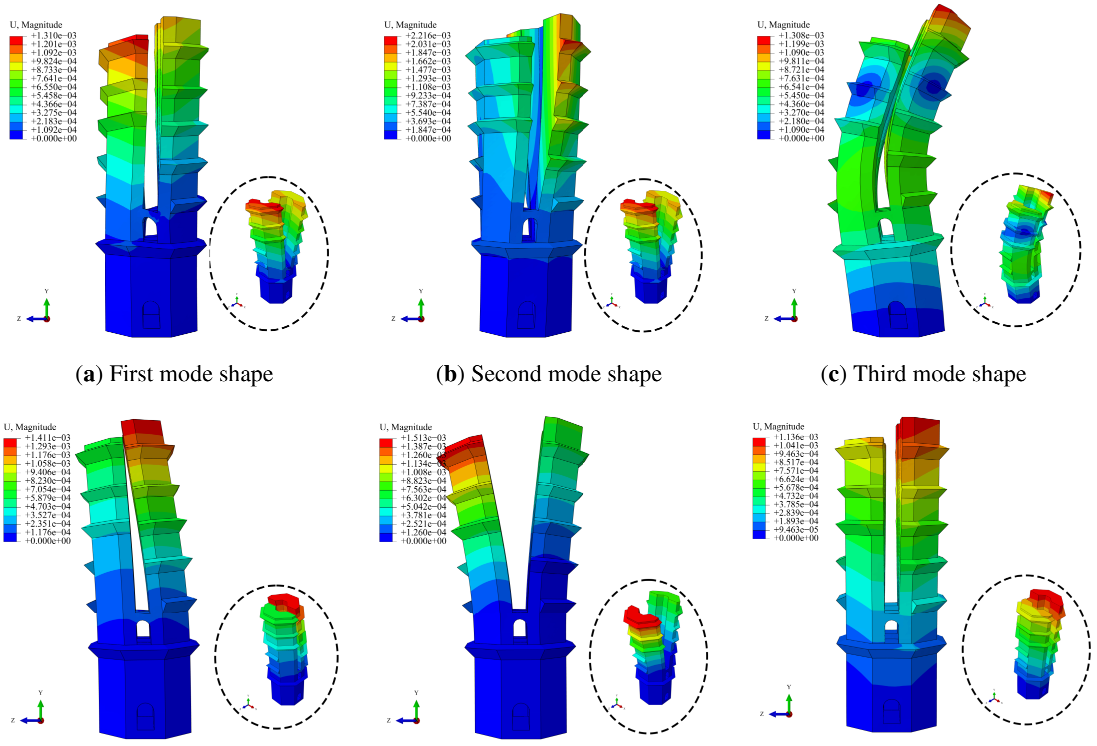

(**a**) First mode shape (**b**) Second mode shape (**c**) Third mode shape

(**d**) Fourth mode shape (**e**) Fifth mode shape (**f**) Sixth mode shape

Figure 4: Structural mode shapes.

Modal analysis results indicate that displacement amplitudes across all modes correspond to bending or torsional vibration patterns. The first mode represents global bending vibration, characterized by lateral sway of the pagoda in the Y or Z direction. The second mode involves higher-order bending in the same direction or incorporates minor torsional components. The fifth mode exhibits a localized vibration mode with pronounced oscillations at the tower's apex or specific stories. Remaining modes demonstrate hybrid vibrations (bending + torsion) or higher-order global modes. It is concluded that lower-order modes (1st–2nd) dominate global bending vibrations, necessitating focused evaluation of wind resistance stability, while higher-order modes (5th–6th) exhibit significant local amplitudes, highlighting regions requiring targeted reinforcement. This study assesses structural safety under actual wind loads through dynamic response analysis.

2.4 Damping Selection

The Rayleigh damping model is a linear damping model that assumes the total damping of a structure is obtained through a linear combination of the mass and stiffness matrices of the structure. It can be expressed by the following equation:

$$[C] = \alpha \times [M] + \beta \times [K] \quad (1)$$

where, $[C]$ is the damping matrix of the structure, $[M]$ is the mass matrix, and $[K]$ is the stiffness matrix. α and β are parameters in the Rayleigh damping model. This paper employs the Rayleigh damping model to account for structural damping, substituting the results of modal analysis into the damping model to calculate the structural damping. The calculation formula is as follows:

$$\alpha = \frac{4\pi\omega_1\omega_2\xi}{\omega_1 + \omega_2} \tag{2}$$

$$\beta = \frac{\xi}{\pi(\omega_1 + \omega_2)} \tag{3}$$

where, α and β denote the mass-proportional and stiffness-proportional damping coefficients, respectively; ω_1 and ω_2 are the first two natural angular frequencies of the structure; ξ is the damping ratio. Considering that the damping ratio of masonry tower structures typically ranges from 0.01 to 0.05, this paper adopts a damping ratio of $\xi = 0.05$ for the tower, resulting in calculated values of $\alpha = 0.35689$ and $\beta = 0.00690$. These parameters are then sequentially imported into the ABAQUS model for subsequent analysis. It should be noted that the damping ratio of $\xi = 0.05$ represents an upper-bound estimate for intact masonry. For a severely damaged structure like this pagoda, the actual damping ratio is likely higher due to increased internal friction at crack interfaces. If a higher damping ratio were employed, the structural response would be reduced. Therefore, the results obtained with $\xi = 0.05$ can be considered conservative estimates for the damaged pagoda. The core conclusions of the study remain robust even if a higher damping ratio were considered.

3 Simulation of Pulsating Wind Using MATLAB

Wind-induced vibration analysis is essential for structural design. To study wind-induced vibrations, accurate wind load time histories are required. However, if the actual measured wind data from site observations are directly applied to the structure, the structural response may not reach its peak before the wind effect diminishes. Therefore, artificial wind simulation is a more feasible approach. Currently, two main methods are employed: the first involves generating wind load time histories using known parameters such as terrain type and wind spectrum characteristics, through which wind velocity is simulated and subsequently converted into wind load acting on the structure [22]. The second method relies on wind tunnel testing, where sensors are used to acquire surface pressure data from the model, and the measured data are then transformed into wind load time histories. This paper adopts the first method—artificial wind simulation. MATLAB is utilized to generate fluctuating wind velocity time histories based on the wind velocity spectrum, yielding realistic fluctuating wind velocities. Through simulation analysis, fluctuating wind pressure time histories are obtained.

3.1 Definition of Fluctuating Wind

The wind speed at any location is composed of both the mean wind speed and the fluctuating wind speed. The mean wind can be regarded as a static component, remaining constant over time, whereas the fluctuating wind is a stochastic dynamic component that varies with time and must be described using statistical methods [23,24]. Fluctuating wind speed can be represented as a zero-mean Gaussian stationary random process, which is ergodic in nature. The power spectral density (PSD) function is the most important statistical characteristic of fluctuating wind, as it indicates the distribution of wind energy across different frequencies. Furthermore, based on actual observations of strong winds, it is known that during a gust event, the wind speed and direction at different positions on the windward surface of a structure can be inconsistent, and may even differ significantly. Therefore, when studying the fluctuating wind speeds at various nodes of an ancient pagoda, the spatial correlation of the fluctuating wind must be taken into account.

3.2 Selection of Wind Spectra and Simulation Methods for Fluctuating Wind

Currently, there are five commonly used fluctuating wind velocity spectra: Davenport, Kaimal, Simiu, Harris, and Karman. The first two are widely applied in the analysis of wind-induced dynamic responses of buildings. The main difference between the Davenport and Kaimal spectra lies in whether the turbulence scale varies with height. The Kaimal spectrum accounts for the influence of height on wind velocity, whereas the Davenport spectrum, which is most widely used in China, does not.

3.2.1 Davenport Wind Velocity Spectrum

The typical characteristic of the Davenport wind velocity spectrum is that the power spectral density of horizontal fluctuating wind remains constant with respect to height [25]. Its mathematical expression is:

$$S_{\text{Davenport}}(f) = \frac{4k \cdot V_{10}^2 \cdot x_n^2}{f \cdot (1 + x_n^2)^{4/3}} \tag{4}$$

where: $S_{\text{Davenport}}(f)$ is the power spectral density of the Davenport wind velocity spectrum; k is the surface roughness coefficient; $V_{10}$is the mean wind speed converted to aheight of 10mabove ground; f is the frequency of the fluctuating wind; $x_n = \frac{1200f}{\bar{v}_{10}}$.

3.2.2 Kaimal Wind Velocity Spectrum

The typical characteristic of the Kaimal wind velocity spectrum is that its power spectral density varies with height [26], and its expression can be simplified as:

$$S_{\text{Kaimal}}(f) = \frac{200 \cdot f_r}{(1 + 50 f_r)^{5/3} \cdot f} \cdot u_*^2 \tag{5}$$

where: $S_{\text{Kaimal}}(f)$ is the power spectral density of the Kaimal wind velocity spectrum; f_r is the relative frequency, defined as $f_r = \frac{f \cdot z}{U(z)}$, where z is the height and $U(z)$ is the mean wind speed at height z; u_* is the friction velocity, calculated using the following formula:

$$u_* = \frac{U(z) \cdot k}{\ln\left(\frac{z}{z_0}\right)} \tag{6}$$

where k is the Kaimal constant, taken as the classical value of 0.4; z_0 is the surface roughness length, determined based on terrain classification.

3.2.3 Simulation Methods for Fluctuating Wind

Considering that the current Chinese wind load code adopts the Davenport wind velocity spectrum, while the Kaimal spectrum accounts for the influence of height on wind speed, both the Davenport and Kaimal spectra are selected in this study to simulate fluctuating wind. The ancient pagoda is located in a terrain category C. Based on its actual design conditions, the mean wind speed at a height of 10 m is taken as 24 m/s, according to the basic wind pressure map specified in the Chinese Load Code for Building Structures (GB50009-2012) [27] and the climatic characteristics of Shanxi Province.

Since the Davenport wind velocity spectrum does not account for the influence of vertical height on the wind spectrum, and actual fluctuating wind is also affected by horizontal position, spatial correlation of fluctuating wind speeds must be considered when using the Davenport spectrum to simulate actual wind speeds in this study. Currently, artificial wind speed time history simulation methods are mainly categorized into two types: the linear filter method and the harmonic superposition method. The linear filter method transforms a zero-mean white noise random sequence through appropriate transformations to generate a random process with specified spectral characteristics, including the autoregressive (AR) model and the autoregressive moving average (ARMA) model [28], and is a conditionally stable simulation method. The harmonic superposition method simulates the wind speed process as the superposition of a series of cosine functions, and is an unconditionally stable high-precision simulation method. Depending on the number of simulation points, it can be divided into single-point and multi-point simulations. To address the low efficiency of traditional harmonic superposition algorithms in simulating multivariate random fluctuating wind fields, Luongo and Zulli [29] employed an optimized algorithm for harmonic superposition. Recently, new simulation methods such as wavelet analysis have also been introduced. In this paper, the harmonic superposition method is employed to generate a random wind field that satisfies the target power spectrum and coherence function by superimposing multiple harmonic components. The main mathematical model is briefly described as follows.

The harmonic superposition method achieves efficient time-domain wind load generation by decomposing the target power spectrum into discrete harmonic components using the inverse fast Fourier transform (IFFT). The specific steps are as follows: (1) Calculate the target power spectral density based on the Davenport or Kaimal spectrum; (2) Construct a cross-spectral matrix incorporating the spatial coherence function, and ensure its positive definiteness through LDL decomposition; (3) Generate complex frequency-domain signals with random phase, convert them to the time domain via IFFT, and eliminate Gibbs phenomena through spectral symmetry extension.

This method reduces the computational complexity of the traditional harmonic superposition method, enabling efficient generation of multi-node wind load time histories that meet code requirements. Consistency with the target spectrum is verified through power spectral comparison (RMS error < 8%), providing a reliable input for subsequent analysis of wind-induced dynamic responses. In this study, MATLAB code is developed using the aforementioned method to simulate fluctuating wind velocities; with the input of relevant simulation parameters, the fluctuating wind speed time histories at each point can be obtained. Below are the core formulas used in the harmonic superposition method.

(1) Harmonic Component Superposition Formula

$$u_i(t) = \sqrt{2} \sum_{k=1}^{N_{\text{freq}}} \sqrt{S_{ii}(f_k)\Delta f} \cdot \cos(2\pi f_k t + \phi_{ik}) \tag{7}$$

where: $S_{ii}(f_k)$ is the target power spectral density; Δf is the frequency resolution, with a sampling frequency of 10 Hz; ϕ_{ik} is the random phase, ensuring the randomness and stationarity of the signal; N_{freq} is the number of harmonics. This formula generates random signals with specified spectral characteristics by superposing discrete spectral components combined with power spectral density and random phase, serving as a core tool for simulating physical random processes.

(2) Spatial Correlation Control (Coherence Function)

$$\text{coh}_{ij}(f) = \exp\left(-\frac{f\sqrt{c_x^2 r_x^2 + c_y^2 r_y^2 + c_z^2 r_z^2}}{\overline{U}_m}\right) \tag{8}$$

where: coh_{ij} is the coherence between nodes i and j; c_x, c_y, c_z are decay coefficients; c_x, c_y, c_z are spatial distances; $\overline{U}_m$ is the mean wind speed.

(3) IFFT Acceleration Formula

$$u(t) = \sqrt{\frac{2}{T}} \cdot \mathrm{IFFT}\left[\sum_{k=1}^{N_{\mathrm{freq}}} \sqrt{S_k} \cdot e^{i\phi_k}\right] \tag{9}$$

3.3 Simulated Fluctuating Wind Field

The residual pagoda model used in this study has a height of approximately 34.1 m. To improve the accuracy of the simulation results, the ancient pagoda model is divided into seven segments according to actual conditions. At the top of each segment, a representative node is defined, and the wind speed time history of that node is applied to all nodes within the same segment. These nodes are located at heights of Node 1 (9.98 m), Node 2 (14.96 m), Node 3 (19.34 m), Node 4 (23.44 m), Node 5 (27.15 m), Node 6 (31.54 m), and Node 7 (34.12 m). Fig. 5 shows the nodes selected for wind speed time history output. Nodes 1 to 7 represent the respective sections from the base to the top of the tower B. By inputting the spatial coordinates of these seven nodes into the MATLAB program, the fluctuating wind speed curves varying with time for each node can be obtained. Adding the corresponding mean wind speed yields the final actual wind speed time history curve. The static wind data for seven nodes are detailed in Table 2. Based on the actual location of the ancient pagoda in this study, the terrain category is classified as Type C. In Type C terrain, the formula for the variation of mean wind speed with height z is given by:

$$v(z) = v_{10}\left(\frac{z}{10}\right)^{0.22} \tag{10}$$

where: v_{10} is the wind speed at a height of 10 m (in this study, the basic wind speed is taken as 24 m/s).

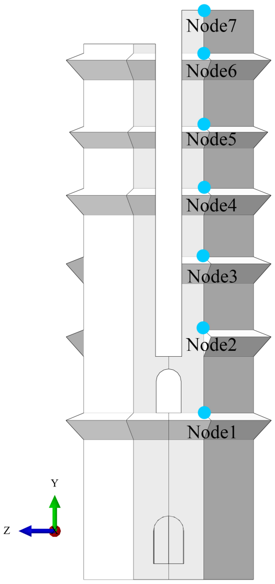

Figure 5: Wind speed output node distribution.

Table 2: Static wind at seven nodes.

Node Number	Static Wind Speed (m/s)	Node Number	Static Wind Speed (m/s)
1	23.99		
2	26.22	5	29.90
3	27.75	6	30.90
4	28.95	7	31.44

Considering spatial correlation, the harmonic superposition method is employed to generate fluctuating wind speed time history curves for seven nodes, using both the Davenport and Kaimal wind velocity spectra. Fig. 5 presents the wind speed time history curves for all nodes based on the Davenport spectrum, representing the actual wind, fluctuating wind, and mean wind acting on each of the seven tower levels.

From the seven nodes shown in Fig. 6a–g, it can be observed that considering spatial height correlation, the fluctuating wind speed time history curves simulated based on the wind velocity spectra are related to the spatial height, and the overall curves change as the spatial position varies. Fig. 6h presents the wind speed power spectral density at the top node of the ancient pagoda. It can be seen that the simulated Davenport wind velocity spectrum is in close agreement with the target spectrum, indicating that the method used to simulate the Davenport spectrum is both feasible and accurate.

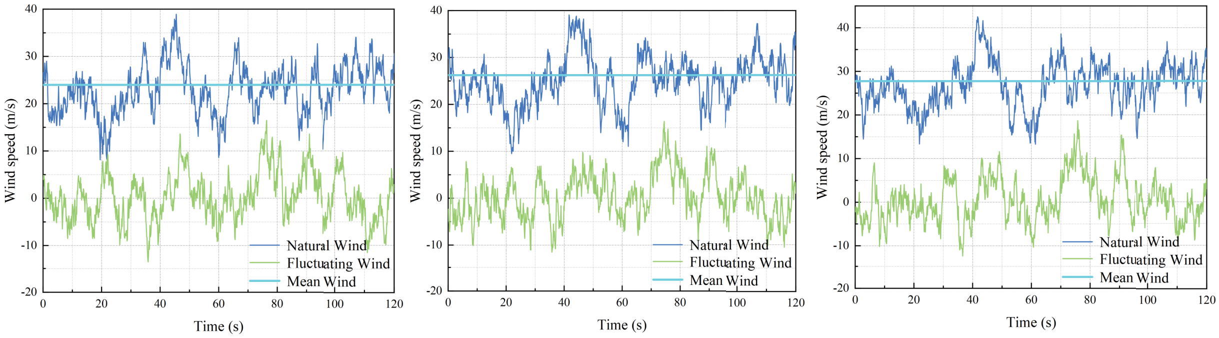

(**a**) Wind speed time history curve at node 1 (**b**) Wind speed time history curve at node 2 (**c**) Wind speed time history curve at node 3

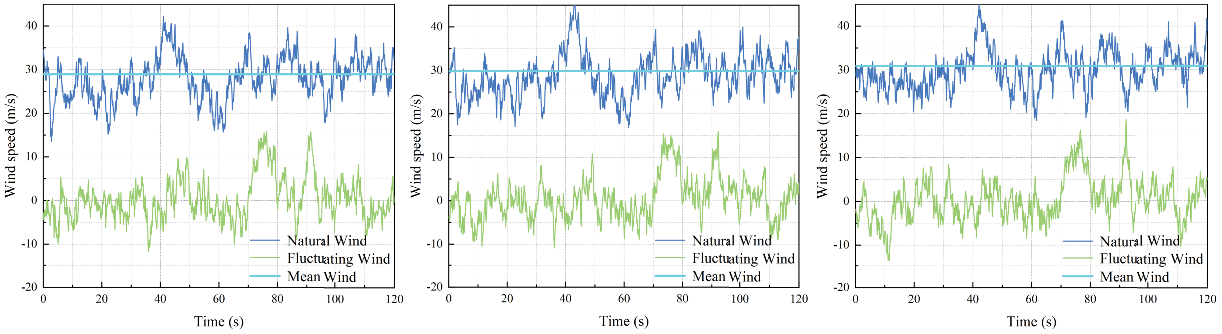

(**d**) Wind speed time history curve at node 4 (**e**) Wind speed time history curve at node 5 (**f**) Wind speed time history curve at node 6

Figure 6: (Continued)

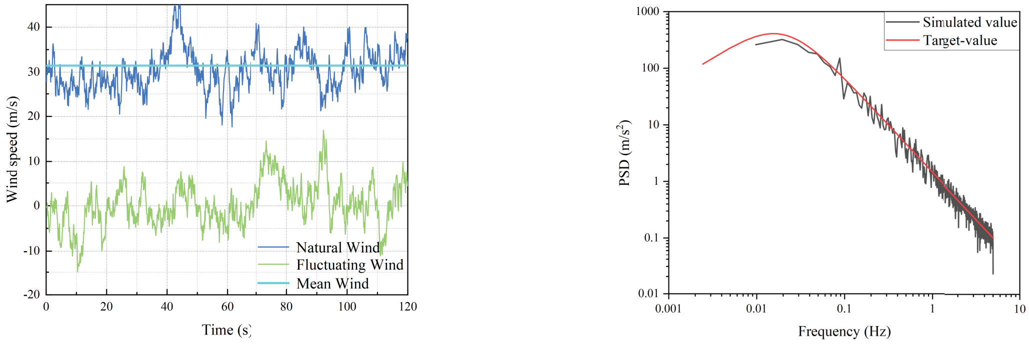

(**g**) Wind speed time history curve at node 7

(**h**) The power spectral density of wind speed at node 7

Figure 6: Davenport wind speed spectrum.

Fig. 7a–g presents the wind speed time history curves for all nodes based on the Kaimal wind velocity spectrum, representing the actual wind, fluctuating wind, and mean wind acting on each of the seven tower levels.

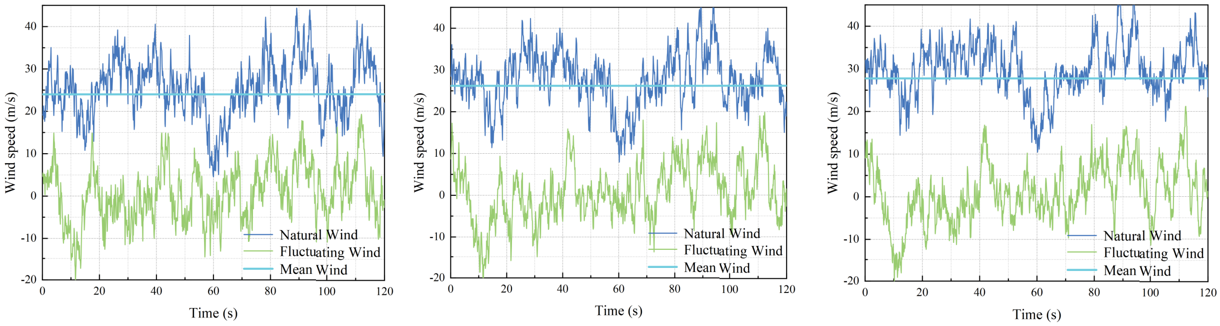

(**a**) Wind speed time history curve at node 1

(**b**) Wind speed time history curve at node 2

(**c**) Wind speed time history curve at node 3

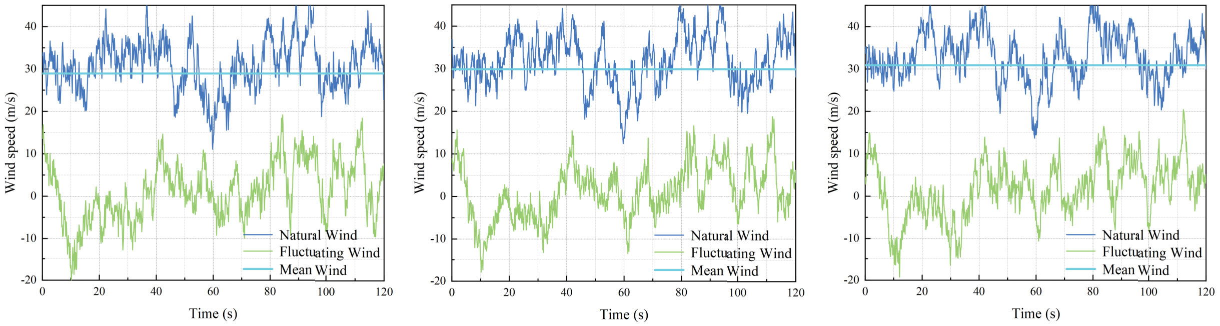

(**d**) Wind speed time history curve at node 4

(**e**) Wind speed time history curve at node 5

(**f**) Wind speed time history curve at node 6

Figure 7: (Continued)

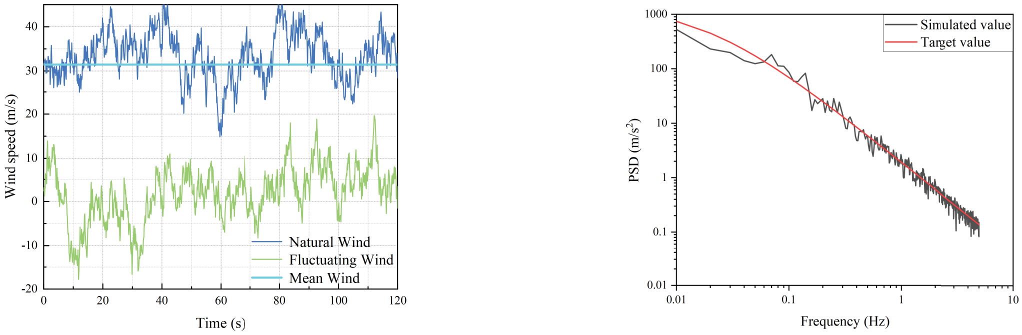

(**g**) Wind speed time history curve at node 7

(**h**) The power spectral density of wind speed at node 7

Figure 7: Kaimal wind speed spectrum.

Fig. 7h shows the wind speed power spectral density at the top node of the ancient pagoda simulated using the Kaimal wind velocity spectrum. It can be observed that the simulated Kaimal spectrum is in close agreement with the target spectrum, demonstrating the feasibility and accuracy of the simulation method. The consistency between the simulated and target power spectra indicates that the wind speed time history calculated using the harmonic superposition method is reliable and effective. Therefore, this method can be applied to numerical simulations of wind-induced vibrations in historic building structures. The following wind-induced response analysis is based on the Davenport wind velocity spectrum.

3.4 The Generation of Pulsating Wind Loads

According to the latest "Load Code for Building Structures" (GB50009-2012), there is a defined relationship between wind speed and wind pressure, with wind pressure being proportional to the square of the wind speed. In this study, the wind speeds at various points on the ancient pagoda are derived based on Bernoulli's equation. By combining the square of the wind speed with the projected area and shape coefficient of the structure, the dynamic wind load is directly computed. The wind load calculation formula for the ancient pagoda is given as follows:

$$W(t) = \frac{1}{2}\rho \cdot u_t(t)^2 \cdot \mu_s \cdot A_s \tag{11}$$

where: $W(t)$ is the wind load time history; ρ is the air density; $u_t(t)$ is the total wind speed time history; μ_s is the shape coefficient; A_s is the projected area.

Taking the wind speed time history curve at Node 117 as an example, which represents the top of the ancient pagoda, the wind speed is converted into wind load acting on the tower top. The time history curve obtained based on the Davenport wind velocity spectrum is shown in Fig. 8a, while the time history curve derived from the Kaimal wind velocity spectrum is shown in Fig. 8b. It is noted that while both Davenport and Kaimal spectra were simulated to validate the reliability of the harmonic superposition method (Figs. 6h and 7h), the subsequent structural response analysis utilized only the Davenport spectrum. This selection aligns with the *Chinese Load Code for Building Structures* (GB50009-2012) and ensures practical applicability. Given that the study focuses on comparative trends across wind directions and reinforcement schemes, the Davenport spectrum provides a consistent and code-compliant basis for the dynamic analysis.

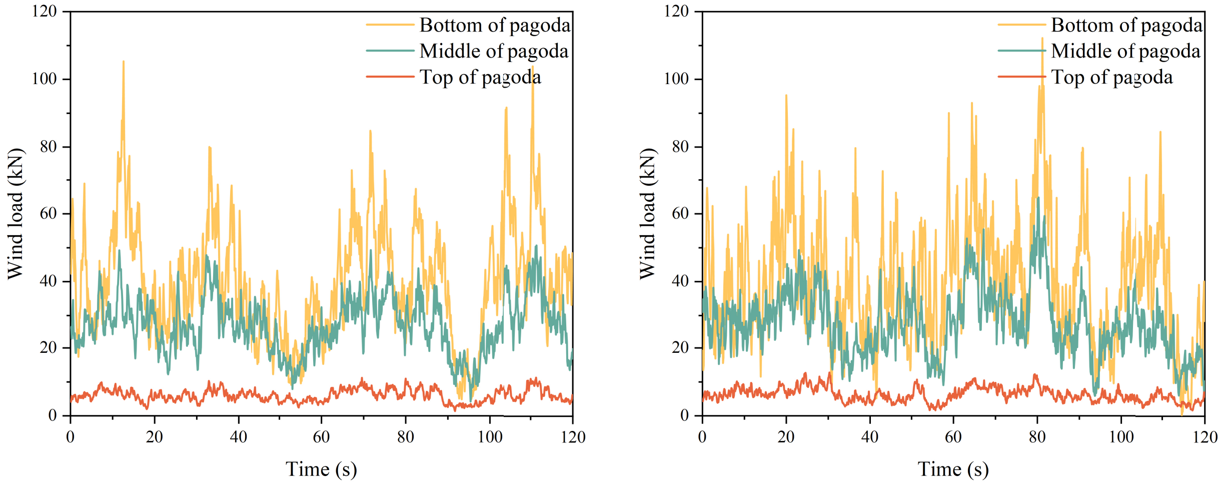

(**a**) Wind load curve based on the davenport spectrum (**b**) Wind load curve based on the kaimal spectrum

Figure 8: Wind load time history curve.

4 Dynamic Response Analysis of the Ancient Pagoda under Fluctuating Wind

4.1 Wind Load Application Method

To account for the asymmetric U-shaped configuration, a Cartesian coordinate system was established consistent with the residual pagoda's geometry (Fig. 9a). The X-axis connects Towers A and B (perpendicular to the opening), the Z-axis parallels the opening, and the Y-axis represents vertical elevation. Two critical wind incidence angles (β) were analyzed:

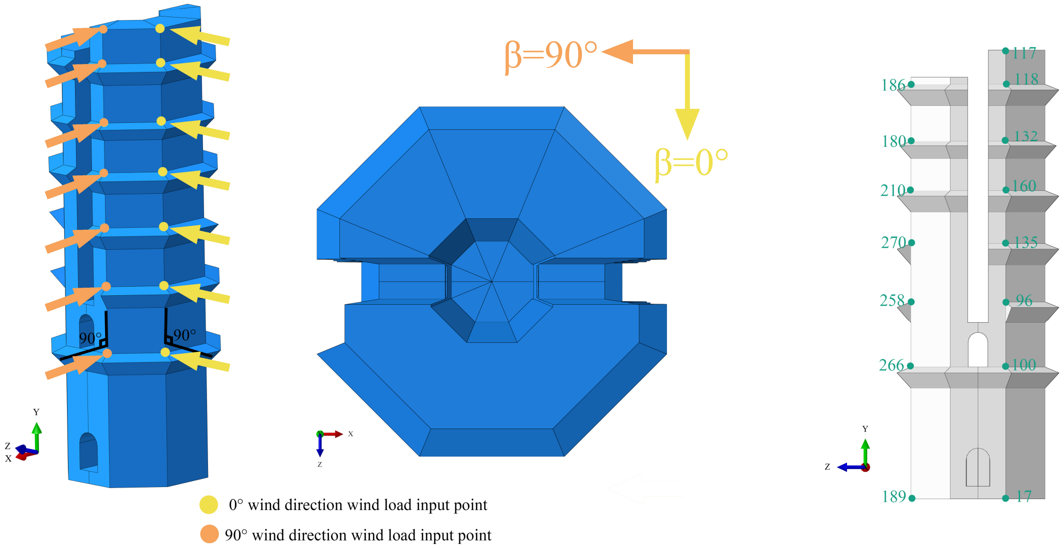

(**a**) Schematic diagram of wind load application points and wind incidence angles (**b**) Result output points

Figure 9: Schematic of input and output nodes and wind incidence angles.

$\beta = 0°$: Wind flows along the positive Z-axis, attacking the side faces of both towers (octagonal facets perpendicular to the X-axis).

$\beta = 90°$: Wind flows along the negative X-axis, directly impinging on Tower B's front face. This creates a channeling effect within the gap, generating significant suction on the inner faces of both towers. This direction was identified as the most critical case due to higher stress concentrations across the damaged interface.

Wind loads were applied as nodal forces based on generated time histories. Fig. 9a illustrates the flow directions relative to the tower plan, while Fig. 9b indicates the specific nodal positions for outputting displacement and stress results during the dynamic analysis.

4.2 Stress Response Analysis under Fluctuating Wind Time History

The time history analysis of the structural response under fluctuating wind lasts for a total of 120 s. Stress distribution contour plots of the ancient pagoda are selected at 30-s intervals to illustrate the stress states at different time points. Fig. 10 shows the stress distribution contour plots at 30, 60, 90, and 120 s, respectively.

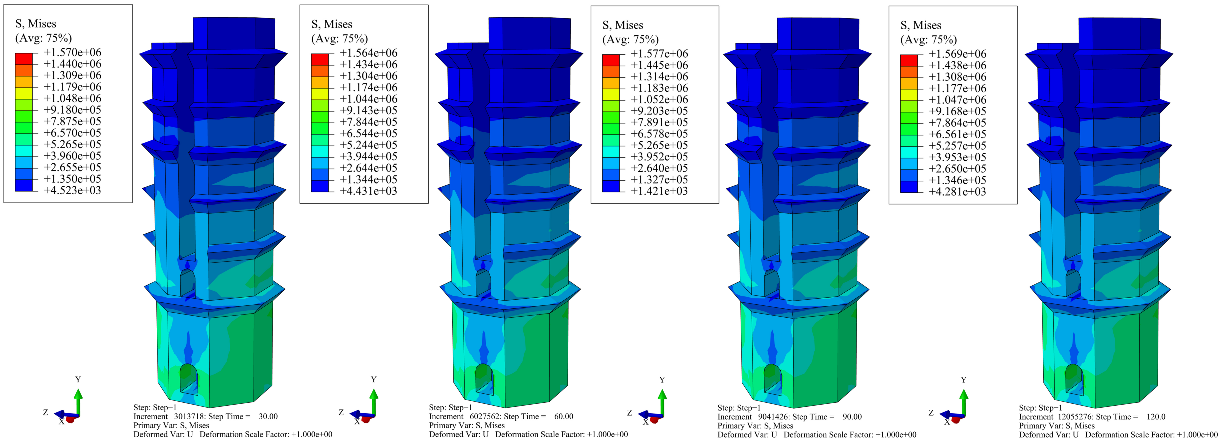

Figure 10: Stress distribution contour plot under a 90° wind incidence angle.

It can be observed from the above figure that the stress amplitude on the surface of the ancient pagoda varies at different time points, but the overall stress distribution pattern remains approximately the same.

4.3 Displacement Response Analysis of the Ancient Pagoda

Through structural time history analysis, the displacement time histories of all nodes in the structure can be obtained. This paper presents the displacement time history curves of key nodes under a 90° wind incidence angle, including Node 186 on Tower A and Node 117 on Tower B at the tower top, as well as Node 266 on Tower A and Node 100 on Tower B at the bottom damaged layer. Fig. 11 shows the displacement time history curves of the top nodes, while Fig. 12 illustrates those of the nodes at the bottom damaged layer. Due to the initial conditions in the numerical simulation—where displacement and velocity are set to zero—and the sudden application of wind load, a brief transient oscillation occurs. The initial seconds of transient data are therefore excluded, and only the response after 20 s is analyzed to ensure stability.

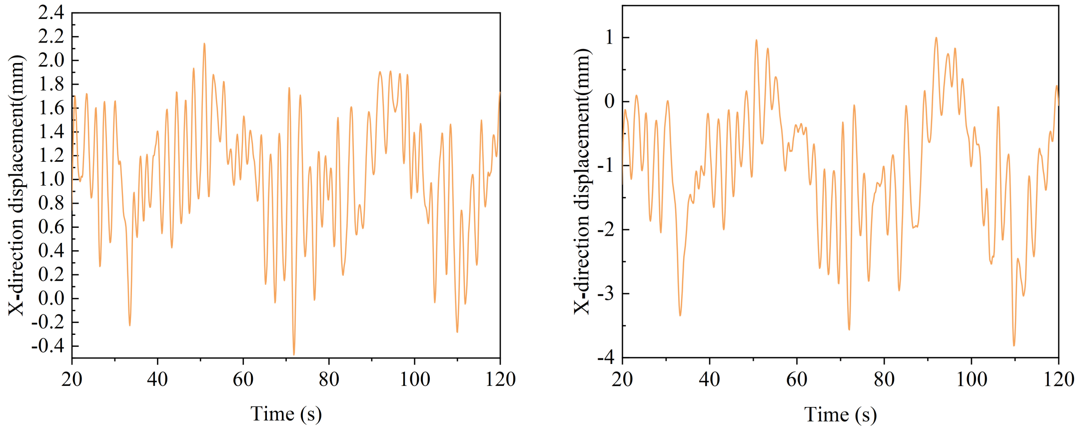

(**a**) *X*-direction displacement time history of node 186 at the top of tower A (**b**) *X*-direction displacement time history of node 117 at the top of tower A

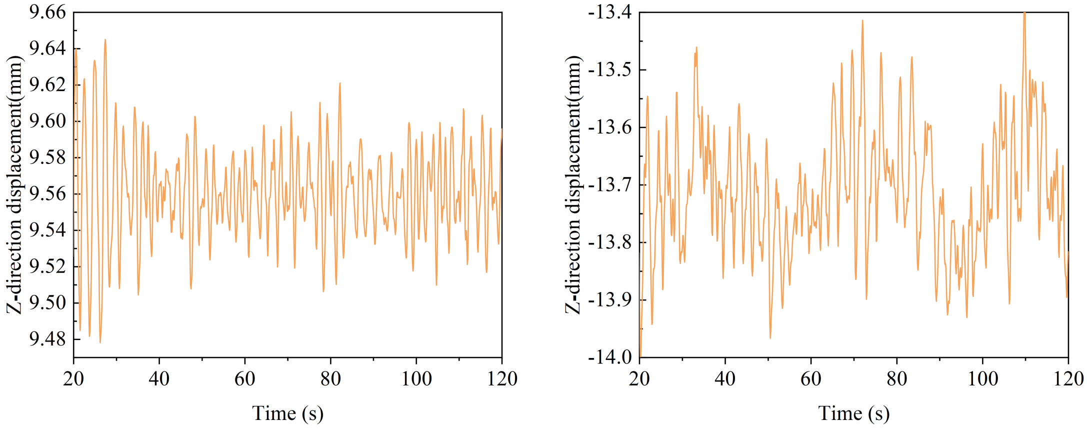

(**c**) *Z*-direction displacement time history of node 186 at the top of tower A (**d**) *Z*-direction displacement time history of node 117 at the top of tower A

Figure 11: Displacement time history curves of top nodes.

From Figs. 11 and 12, it can be observed that the displacement time history curves of Towers A and B are consistent, whether at the top layer or starting from the bottom damaged section. This is closely related to the fluctuating wind speed time history acting on the ancient pagoda. Throughout the fluctuating wind process under a 90° wind incidence angle, the maximum *X*-direction displacement at the top of Tower A is 2.144 mm, while that at Tower B is 3.814 mm. The maximum *Z*-direction displacement at the top of Tower A is 9.645 mm, and at Tower B is 13.998 mm. At the bottom damaged layer, the maximum *X*-direction displacement of Tower A is 0.678 mm, and of Tower B is 0.700 mm; the maximum *Z*-direction displacement of Tower A is 0.934 mm, and of Tower B is 0.844 mm. These results indicate that under a 90° wind incidence angle, the main displacement direction across the ancient pagoda occurs in the *Z*-direction, with significantly larger *Z*-direction displacements compared to those in the *X*-direction. By comparing the displacements at the top nodes and those at the bottom damaged layer, it is evident that the displacements at the pagoda top are considerably greater than those at the damaged layer. This aligns with the theoretical expectation that maximum displacement in an ancient pagoda occurs at the top, following the general rule that displacement increases with height along the pagoda structure.

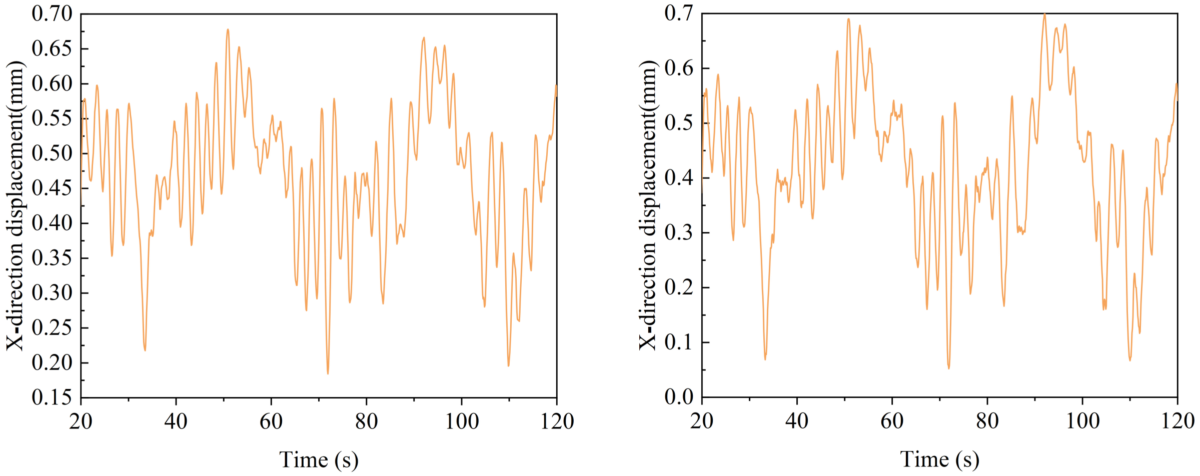

(**a**) *X*-direction displacement time history of node 186 at the top of tower A

(**b**) *X*-direction displacement time history of node 117 at the top of tower A

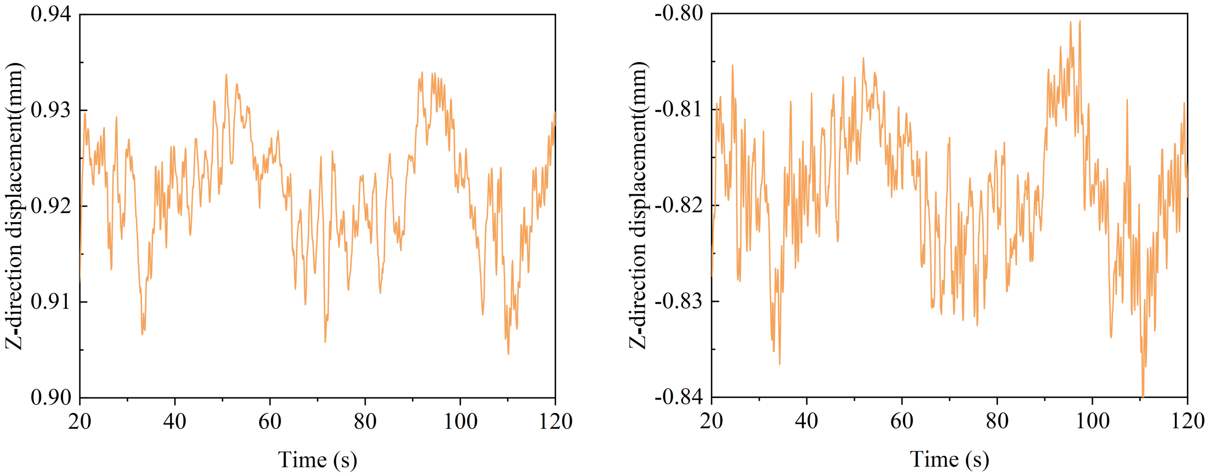

(**c**) *Z*-direction displacement time history of node 186 at the top of tower A

(**d**) *Z*-direction displacement time history of node 117 at the top of tower A

Figure 12: Displacement time history curves of nodes at the bottom damaged layer.

To assess the engineering significance of the calculated displacements, the maximum *Z*-direction displacement of 14 mm at the top of Tower B is evaluated against established performance criteria. The corresponding global drift ratio is 14 mm/34,100 mm = 0.041% (approximately 1/2436). This value is well below typical thresholds for ancient masonry pagodas, where the serviceability limit state corresponds to an interstory drift ratio of 1/500 (approximately 68 mm for this height). For historical masonry more broadly, global drift ratios between 0.01% and 0.07% are associated with negligible damage. The visible damage shown in Fig. 10 is primarily attributed to the 1303 earthquake and long-term degradation, not to current wind loads. The wind-induced displacements are two orders of magnitude smaller than critical values that would initiate new damage.

4.4 Dynamic Response Analysis under Different Wind Incidence Angles

To investigate the effect of different wind incidence angles on the dynamic response of the residual pagoda, displacement time history analyses are conducted under wind incidence angles of 90° and 0°. Fig. 13

shows the variation of X-direction and Z-direction displacements at various nodes along the pagoda height under the two wind incidence angles.

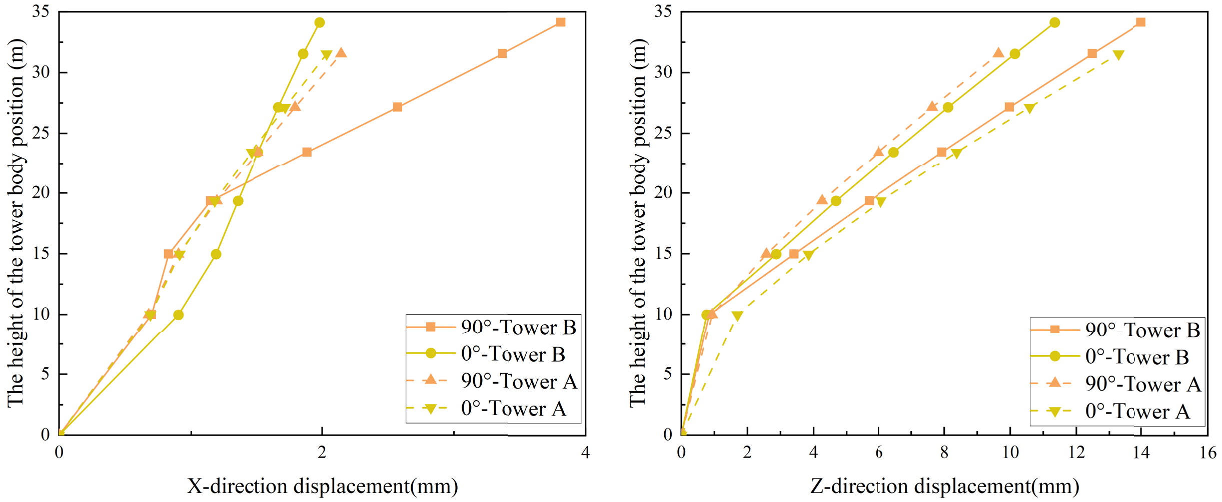

(**a**) X-direction displacement of all nodes (**b**) Z-direction displacement of all nodes

Figure 13: Displacement variation with height.

From Fig. 13, it can be observed that under different wind incidence angles, both the X-direction and Z-direction displacements of the pagoda nodes increase with height. In terms of the X-direction displacement, the overall displacement fluctuates less compared to that in the Z-direction. Under a 90° wind incidence angle, the displacement values of Tower B are the largest among all four curves, with a maximum displacement of 3.814 mm. Regarding the Z-direction displacement, the four curves show a relatively consistent trend. Under a 90° wind incidence angle, Tower B exhibits the largest overall displacement, whereas under a 0° wind incidence angle, Tower A shows greater displacement than under 90°, indicating a stronger wind-induced vibration response of Tower A at 0°. Overall, the 90° wind incidence angle represents the most unfavorable wind direction for the wind-induced vibration characteristics of the residual pagoda, under which the maximum displacement response occurs.

5 CFRP Material Reinforcement

5.1 Introduction to CFRP

Carbon fiber reinforced plastic (CFRP) is a high-performance composite material widely used in the field of civil engineering due to its lightweight, high strength, high stiffness, and excellent corrosion resistance [30]. The strength and stiffness of CFRP materials are significantly higher than those of traditional reinforcing materials [31], making them highly advantageous for reinforcing concrete structures. CFRP reinforcement technology is primarily applied to concrete structural surfaces through external bonding [32,33] or wrapping [34], utilizing the high tensile strength of CFRP to share the tensile stress in the structure, thereby enhancing its load-carrying capacity and stiffness.

The CFRP material is modeled with C3D8R solid elements, which are 8-node linear brick elements with reduced integration. This element type can accurately simulate the three-dimensional mechanical properties of CFRP, and has good compatibility with the C3D8R solid elements used for the masonry pagoda model, ensuring the convergence and accuracy of the numerical calculation. The Tie constraint is adopted to simulate the bonding interface. The surface of the masonry pagoda where CFRP is pasted is defined as the master surface, and the inner surface of the CFRP solid element is defined as the slave surface. All translational and rotational degrees of freedom of the two surfaces are tied, assuming perfect bonding at the interface without considering debonding failure. This setting is a common and reasonable simplification in the numerical simulation of CFRP-reinforced masonry structures, which is based on the fact that the CFRP reinforcement in this study is designed with sufficient bonding length and reliable interface treatment, and debonding is not the main failure mode of concern.

5.2 Reinforcement Scheme

Based on the stress contour analysis of the pagoda structure presented earlier, the critical reinforcement zones can be identified. As shown in Fig. 14, these zones are reinforced through the external application of carbon fiber-reinforced polymer (CFRP) materials. This method not only significantly enhances the structural stability of the ancient pagoda but also effectively reduces the principal tensile stresses in the pagoda body, thereby providing an additional protective layer to the masonry blocks and limiting their displacement under tension, as well as preventing them from reaching their uniaxial tensile strength limit. This reinforcement approach also preserves the original historical appearance of the pagoda. Due to its excellent mechanical properties and ease of installation, CFRP is widely used in the reinforcement of historic buildings. According to [35] the material properties of CFRP are as listed in Table 3, which make it an ideal reinforcing material. The application process has minimal impact on the original structure of the pagoda, reducing the risk of secondary damage and ensuring the reversibility of the reinforcement work, thus offering an effective solution for the long-term preservation of the ancient pagoda.

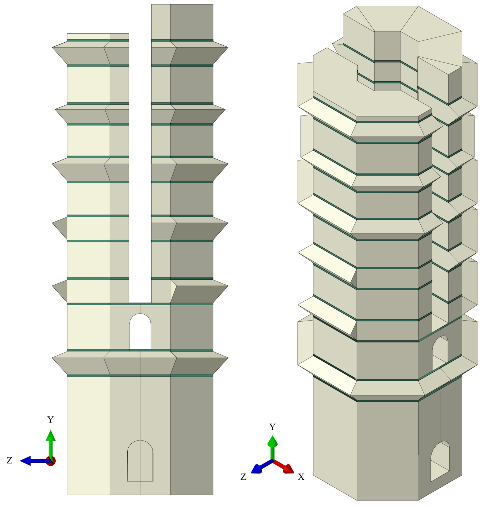

● CFRP strengthening configurations of pagoda

(a) 2D diagram of ancient pagoda reinforcement (b) 3D diagram of ancient pagoda reinforcement

Figure 14: Schematic diagram of reinforcement locations.

Table 3: Material properties of CFRP.

Materials	Tensile Strength (MPa)	Elasticity Modulus (GPa)	Thickness (mm)
CFRP	4400	255	0.34

In the finite element model, the CFRP was simulated using solid elements and bonded to the masonry surface with a Tie constraint in ABAQUS, assuming perfect bond with no relative slip. This simplification was adopted for computational efficiency and due to the lack of experimental data on the CFRP-masonry bond behavior for this specific structure. It should be noted, however, that this assumption may overestimate the reinforcement effectiveness, as it precludes the possibility of debonding that could occur in reality, particularly around stress concentration areas. The reported displacement reductions should therefore be viewed as upper-bound estimates.

5.3 Damage Analysis of the Ancient Pagoda after Reinforcement

Fig. 15 presents a comparison of the stress contour plots before and after reinforcement under a 90° wind incidence angle. Fig. 16 shows the corresponding damage contour plots. In the wind load simulation, stress analysis was conducted on the residual pagoda both before and after reinforcement with CFRP material, visually demonstrating the effectiveness of the reinforcement.

Using finite element software to simulate wind loads, comparisons of stress contour plots, stress values at critical locations, and stress distribution patterns between the original and CFRP-reinforced structures indicate that CFRP reinforcement effectively reduces stress at key areas, optimizes stress distribution, and enhances the structure's wind-resistant stability.

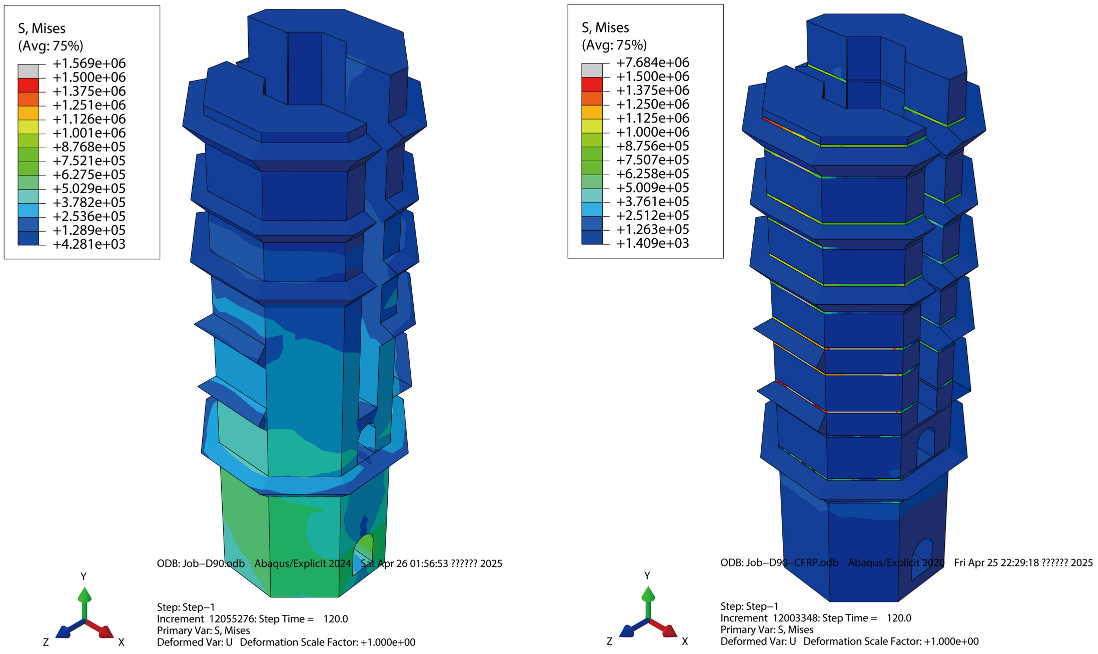

(**a**) Stress contour before reinforcement (**b**) Stress contour after reinforcement

Figure 15: Stress comparison before and after reinforcement.

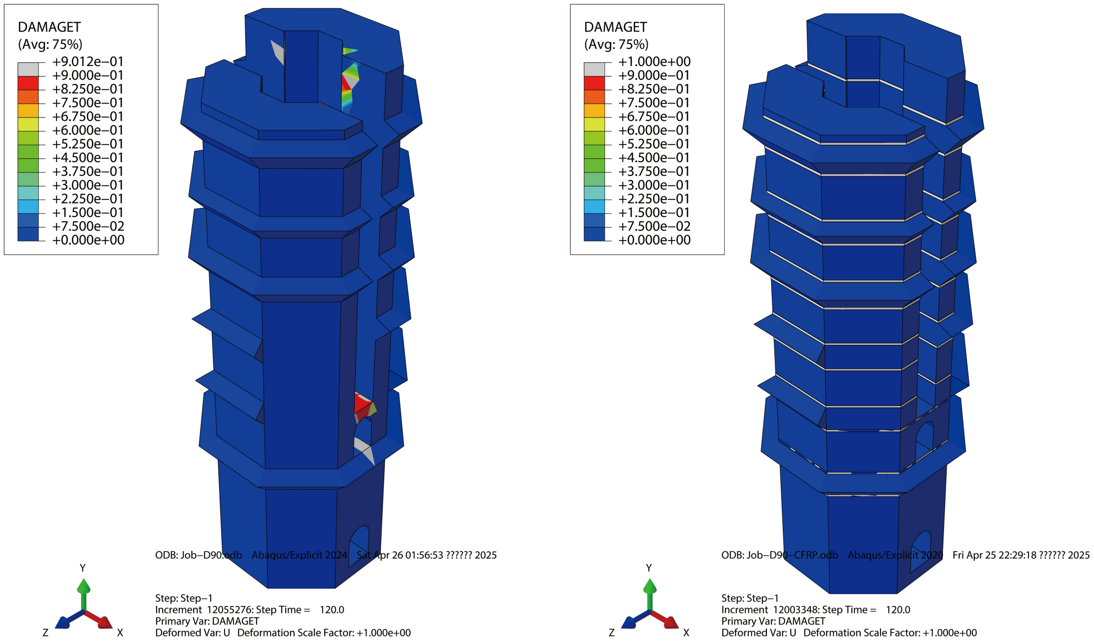

(**a**) Damage contour cefore reinforcement (**b**) Damage contour after reinforcement

Figure 16: Damage comparison before and after reinforcement.

Under wind loading, the original structure exhibits uneven stress distribution. The windward and side surfaces are subjected to direct wind pressure, resulting in stress concentration around door openings, pagoda corners, and damaged regions. These areas experience significantly higher stress levels due to structural discontinuities and abrupt stiffness changes. For instance, under certain wind speeds, the stress at door corners may reach the tensile strength limit of the masonry material, potentially leading to crack propagation and brick loosening, thereby threatening structural safety. As wind speed increases, the area of stress concentration expands and stress levels continue to rise, increasing the risk of structural failure.

After CFRP reinforcement, stress distribution is significantly improved. With its high tensile strength and elastic modulus, CFRP works synergistically with the pagoda body to effectively share the tensile stresses induced by wind loads. On the windward face, CFRP carries part of the tensile stress generated by wind pressure, thereby reducing the tensile stress level in the masonry and minimizing the risk of crack initiation and propagation. Stress at critical locations is greatly reduced—for example, the stress at door corners under the same wind speed may fall within the safe stress range of the masonry material. The area of stress concentration is reduced, and stress distribution becomes more uniform, enhancing the overall wind-resistant stability of the structure and ensuring more reliable performance under wind loads.

5.4 Dynamic Response Analysis under Different Wind Incidence Angles

To investigate the effect of different wind incidence angles on the dynamic response of the residual pagoda after CFRP reinforcement, displacement response analyses are conducted under wind incidence angles of 90° and 0°. Fig. 17 shows the variation of X-direction and Z-direction displacements at various nodes along the height of Towers A and B under the two wind incidence angles.

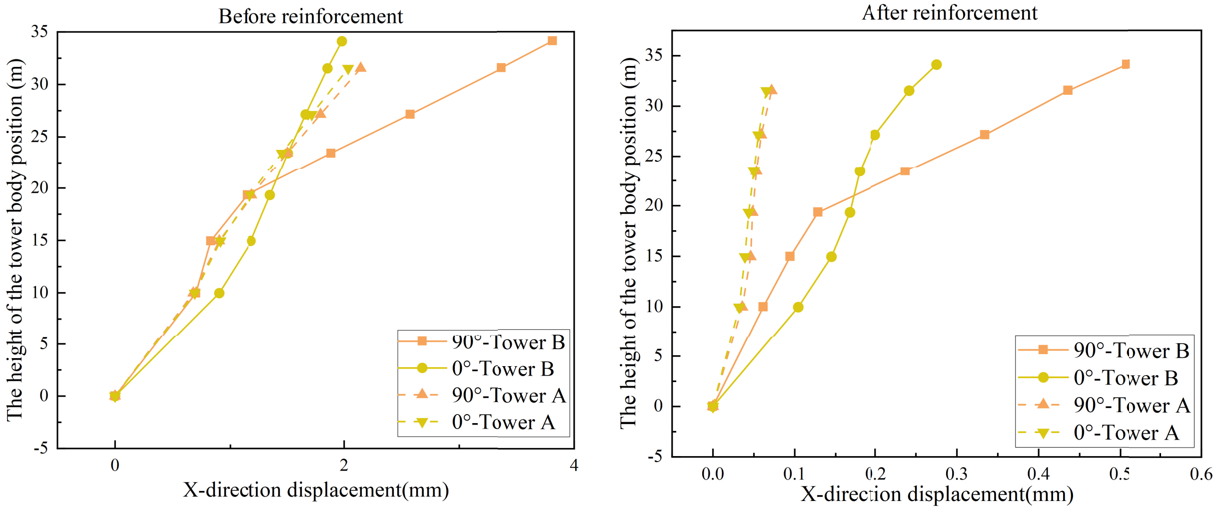

(**a**) Variation of *X*-direction displacement with tower height before and after reinforcement

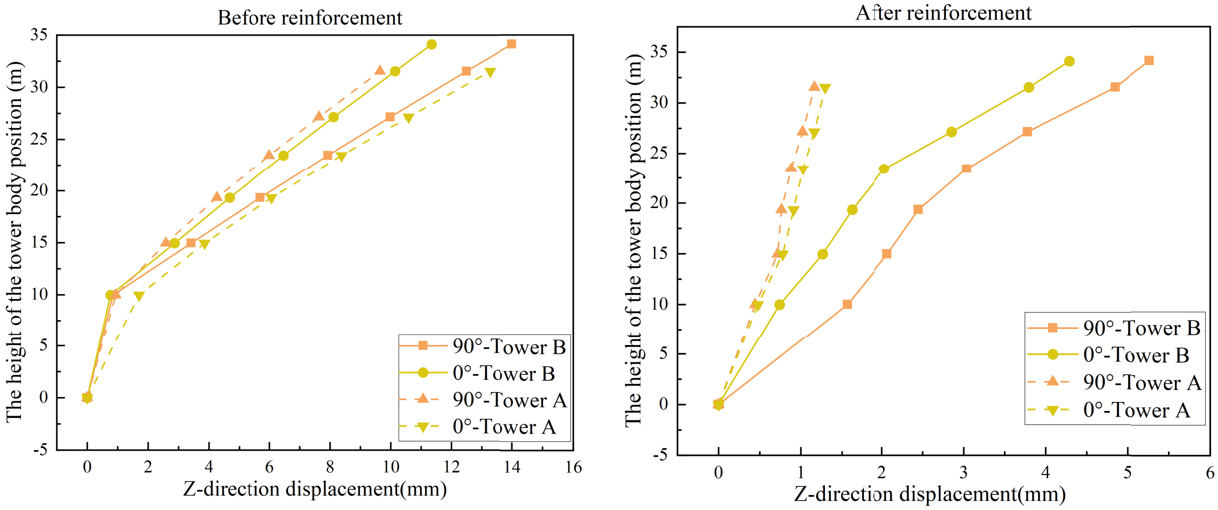

(**b**) Variation of *Z*-direction displacement with tower height before and after reinforcement

Figure 17: Comparison of displacement variation with height at all nodes before and after CFRP reinforcement.

From Fig. 17, it can be observed that after reinforcement, both the *X*-direction and *Z*-direction displacements of the pagoda nodes are significantly reduced, while the overall displacement trend remains relatively consistent with that before reinforcement. In terms of *X*-direction displacement, the displacement response at the top node of Tower B under a 90° wind incidence angle reaches 0.508 mm, while that of Tower A is 0.0716 mm. As shown in the figure, Tower B exhibits larger overall displacement, which aligns with the actual condition that Tower B is taller and thus more affected by wind action. Additionally, under a 0° wind incidence angle, the displacements at three nodes located at heights of 9.98, 14.96, and 19.34 m on Tower B exceed those under the 90° wind incidence angle. However, for nodes above 23.44 m, the displacements under the 90° wind incidence angle gradually become greater than those under 0°, which is consistent with real-world behavior. Regarding the *Z*-direction displacement, the displacement response at the top node of Tower B under a 90° wind incidence angle reaches 5.265 mm, while that of Tower A is 1.164 mm. The figure indicates that the displacement responses of Tower A under both wind incidence angles are relatively small, whereas the overall displacement response of Tower B under the 90° wind incidence angle is significantly higher. This increase becomes more pronounced with rising height, which corresponds to actual conditions and confirms the feasibility of CFRP reinforcement. Therefore, the application of CFRP materials plays a crucial role in the protection and structural enhancement of historic buildings.

6 Discussion

This study focuses on a masonry ancient pagoda and conducts wind-resistant performance analysis using the ABAQUS finite element software. Through modal analysis, the first six vibration modes of the structure were obtained, clarifying its fundamental dynamic characteristics. By integrating MATLAB programming to generate fluctuating wind speed time histories and applying the harmonic superposition method to simulate wind pressure loads, the structural response under realistic wind environments was effectively modeled. During MATLAB programming, spatially non-uniform wind field characteristics were incorporated, including vertical variation of mean wind speed, spatial coherence among multi-point wind speeds, and construction of the cross-spectral matrix, thereby enhancing the realism of wind load distribution. This modeling approach significantly improves the accuracy of numerical simulations and constitutes one of the key technical highlights of this study.

In the time history response analysis, noticeable displacement fluctuations were observed during the initial stage (e.g., the first 20 s), primarily due to the transient nature of wind loading, the initial structural state, and the integration algorithm used in numerical computation. As the excitation progressed, the response gradually stabilized, indicating that the structure can adapt to sustained wind loads and enter a quasi-steady vibration state.

Time history analyses under two typical wind incidence angles (0° and 90°) revealed that the 90° wind direction represents the most unfavorable loading condition for the pagoda, with maximum dynamic responses, particularly in the Z-direction displacement, which increases significantly with height. This finding warrants further physical interpretation. The identification of the 90° wind incidence angle as the most unfavorable condition can be attributed to two physical mechanisms. First, aerodynamic interference: at 90°, the wind interacts with the U-shaped plan configuration, creating a "channeling effect" between Towers A and B. This increases the spatial correlation of wind pressures on the two towers, causing them to vibrate in phase and thus excite the global modes of the residual structure more effectively than the 0° case, where shielding effects dominate. Second, damage-excitation coupling: the primary damage zones (door openings and cracks) are oriented such that the Z-direction bending/torsional deformations induced by the 90° wind directly engage these weakened areas, leading to localized nonlinearity and amplified overall displacement. Therefore, the 90° case maximizes both the aerodynamic loading efficiency and the utilization of structural vulnerabilities.

To further enhance the structural safety of the residual pagoda, CFRP materials were introduced for reinforcement simulation. The results show that CFRP reinforcement effectively improves the overall mechanical behavior of the structure, significantly reducing displacement responses and stress concentrations at critical nodes, thereby enhancing structural stability and load-bearing capacity. Due to its advantages of lightweight and high strength, as well as ease of installation, CFRP proves to be an ideal material for reinforcing masonry historical structures without compromising their original appearance. However, the reinforcement alters the original stiffness distribution of the structure, potentially affecting its dynamic characteristics. Therefore, in practical engineering applications, the coordination between reinforcement effectiveness and dynamic response should be carefully considered to ensure both structural safety and preservation of historical authenticity.

Another limitation pertains to the selection of the damping ratio. In Section 2.4, a damping ratio of $\xi = 0.05$ was adopted for the Rayleigh damping model, based on the typical range for masonry structures (0.01–0.05) suggested in the literature. This value represents an upper-bound estimate for intact masonry. However, the subject of this study is a severely damaged (residual) pagoda with pre-existing cracks and local failures. For such damaged masonry structures, the actual damping ratio is likely to be higher due to increased internal friction, crack closure, and energy dissipation at the interfaces of damaged blocks. If a higher damping ratio (e.g., $\xi = 0.08$ or 0.10) were employed, the structural response—particularly the displacement amplitudes shown in Figs. 11–13—would likely be reduced. Consequently, the displacement and stress values presented in this study, which were obtained using $\xi = 0.05$, can be considered conservative estimates for the damaged pagoda. The core conclusions of the paper, namely that the Z-direction displacement dominates, the 90° wind incidence angle is the most unfavorable condition, and CFRP reinforcement effectively mitigates wind-induced vibrations, remain robust even if a higher damping ratio were considered.

While this study provides valuable insights into the structural behavior and reinforcement strategies for the ancient pagoda, several constraints and approximations should be acknowledged.

One primary limitation lies in the material modeling. Capturing the exact nonlinear behavior of ancient masonry is inherently challenging. In this work, the Concrete Damaged Plasticity (CDP) parameters were calibrated based on existing literature rather than direct material-specific tests, which was due to the practical difficulties in sampling historical structures. While this approach aligns with common practices, it may introduce some uncertainty when predicting localized damage patterns.

Another approximation involves the wind load simulation. This study employed a decoupled approach, analyzing the forced vibration response under fluctuating wind loads generated via the harmonic superposition method, rather than fully coupling wind-structure interaction (FSI). For stiff masonry structures under service-level winds, this method is generally acceptable. However, the residual pagoda's asymmetric U-shaped geometry creates a complex aerodynamic environment. Specifically, unbalanced pressures on Towers A and B could induce torsional loads that the current along-wind simulation does not fully capture. This is particularly relevant under the critical 90° wind direction, where torsional effects might exacerbate stress concentrations at the tower interfaces and around existing openings. While the current model effectively identifies the primary buffeting response and the most unfavorable wind angle, future work should consider CFD-based FSI simulations or aeroelastic wind tunnel tests to quantify these torsional components more accurately.

Additionally, the initial smoothing of the wind speed time-history could be further refined. Some response fluctuations were observed within the first 20 s of the analysis, suggesting that the transition from static to dynamic loading was not perfectly seamless. Integrating field measurement data in future studies would help calibrate the wind field model and minimize these initial numerical artifacts.

It is also worth discussing how the findings of this study might apply to other masonry pagodas with different geometries, damage states, or material properties. The identification of 90° as the critical wind direction is largely specific to the U-shaped cross-section of this pagoda, where a channeling effect occurs between the two towers. For symmetric pagodas (e.g., octagonal or circular), the critical wind direction would likely depend on features such as door openings and eaves. However, the underlying principle—that asymmetric geometries can induce torsional responses and that wind directions maximizing spatial correlation are most critical—is broadly applicable. The finding that CFRP reinforcement effectively reduces stress concentrations in damaged regions is highly generalizable and consistent with the wider literature on masonry strengthening. But the optimal reinforcement configuration would need to be tailored to the specific damage pattern of each structure. Similarly, the qualitative conclusion that CFRP reduces wind-induced displacements should hold across different masonry types, though the quantitative reductions would vary with material stiffness, and the CDP parameters would require recalibration for other materials.

Future investigations addressing these aspects—particularly refined material testing and coupled FSI analysis—will offer more robust technical support for the conservation and reinforcement of similar historical masonry structures.

7 Conclusions

This study investigated the dynamic response of a residual ancient brick pagoda under wind loads using numerical simulation. To simulate fluctuating wind speed time histories, the harmonic superposition method was adopted and implemented through MATLAB based on both the Davenport and Kaimal wind velocity spectra. The reliability of the simulated wind speeds was verified and subsequently applied to a finite element model of the ancient pagoda using ABAQUS for dynamic response analysis. The influence of different wind incidence angles on the structural behavior of the residual pagoda was also examined. Finally, CFRP materials were used to reinforce the damaged sections of the pagoda, followed by dynamic characteristic analysis of the reinforced model. Based on the above work, the following conclusions are drawn:

(1) According to the principle of harmonic superposition, a MATLAB-based program was developed to simulate fluctuating wind speeds at multiple spatial points. By extracting and comparing auto-power spectra and cross-power spectra from the simulation results, good agreement was observed between simulated and target spectra. This further validated the feasibility of the developed program and confirmed the accuracy of the fluctuating wind simulation, demonstrating its applicability in ABAQUS finite element analysis.

(2) A refined finite element model of the residual pagoda was established, and wind loads were calculated and applied according to relevant design codes. Frequency characteristics of displacement time history curves were analyzed. Under wind incidence angles of 0° and 90°, six nodes on Tower A and seven nodes on Tower B were selected for detailed investigation. Using ABAQUS explicit dynamics, displacement time history curves of each node under a 90° wind incidence angle were obtained. Dynamic response analysis revealed that the overall displacement response of the residual pagoda is predominantly in the Z-direction, with displacement increasing along the tower height. The 90° wind incidence angle was identified as the most unfavorable condition, under which the maximum dynamic response occurs.

(3) CFRP materials were applied to reinforce the residual pagoda. Post-processing analysis in ABAQUS was conducted on the reinforced model, and comparisons with stress and damage states before reinforcement were made. Results show a significant reduction in structural damage, along with notable improvements in displacement and stress distribution. This confirms the feasibility and effectiveness of using CFRP for reinforcing ancient masonry pagodas, making it a promising approach for the preservation of historic structures.

Acknowledgement: Not applicable.

Funding Statement: The authors received no specific funding for this study.

Author Contributions: Conceptualization, Jia Wang; methodology, Jia Wang; software, Jia Wang; validation, Jiayu Zhou and Kangjie Ling; formal analysis, Jia Wang; investigation, Jia Wang; resources, Jiayu Zhou; data curation, Jia Wang; writing—original draft preparation, Jia Wang; writing—review and editing, Dewen Liu and Chenghao Xu; visualization, Jia Wang; supervision, Dewen Liu and Chenghao Xu; project administration, Dewen Liu and Chenghao Xu. All authors reviewed and approved the final version of the manuscript.

Availability of Data and Materials: Data available on request from the authors.

Ethics Approval: Not applicable.

Conflicts of Interest: The authors declare no conflicts of interest.

References

1. Athanasiou A, Tirca L, Stathopoulos T. Scaling wind loads for incremental dynamic analysis applications. J Wind Eng Ind Aerodyn. 2025;263(8):106116. doi:10.1016/j.jweia.2025.106116.
2. Tian G, Geng D, Wang LL, Stathopoulos TT, Wan M, Chen S. Influence of blockage ratios in shaping wind dynamics in urban environments. J Wind Eng Ind Aerodyn. 2025;257(8):106008. doi:10.1016/j.jweia.2025.106008.
3. Löhner R, Haug E, Michalski A, Muhammad B, Drego A, Nanjundaiah R, et al. Recent advances in computational wind engineering and fluid-structure interaction. J Wind Eng Ind Aerodyn. 2015;144(2):14–23. doi:10.1016/j.jweia.2015.04.014.
4. Asteris PG, Chronopoulos MP, Chrysostomou CZ, Varum H, Plevris V, Kyriakides N, et al. Seismic vulnerability assessment of historical masonry structural systems. Eng Struct. 2014;62(79):118–34. doi:10.1016/j.engstruct.2014.01.031.
5. Li Y, Sun PP, Li A, Deng Y. Wind effect analysis of a high-rise ancient wooden tower with a particular architectural profile via wind tunnel test. Int J Archit Herit. 2023;17(3):518–37. doi:10.1080/15583058.2021.1938748.
6. Li Y, Deng Y, Li A, Xu T. Comparative studies of computational fluid dynamic geometric models at multiple levels of details in evaluating wind action on Asian ancient wooden tower. Int J Archit Herit. 2023;17(6):970–87. doi:10.1080/15583058.2021.2003911.
7. Wu X, Lu J, Wang Z, Yang W, Qiao N. Dynamic characteristics and seismic response analysis of the bottle-shaped masonry ancient pagoda. Structures. 2022;44(2):1648–59. doi:10.1016/j.istruc.2022.08.109.
8. Li Y, Deng Y, Li A. A nondestructive method for controlling wind loads and wind-induced responses of wooden pagoda. Wind Struct. 2022;34(5):525–38. doi:10.1061/jpcfev.cfeng-4786.
9. Tan J, Tan P, Wu J, Feng D. Evaluation of wind-induced fragility and cumulative fatigue damage on seismically isolated high-rise building. J Wind Eng Ind Aerodyn. 2024;254(5):105915. doi:10.1016/j.jweia.2024.105915.
10. Lu J, Tian J, Wang Z, Jiang F, Wu X. Analysis of seismic damage and seismic capacity of the structure of the ultrahigh pagoda. Struct Des Tall Spec Build. 2024;33(17):e2181. doi:10.1002/tal.2181.
11. Al-Azri NMN, Kuckian S, Gaur H. Reducing the impact of wind load with shape of high rise buildings. J Stud Res. 2019;1–12. doi:10.47611/jsr.vi.933.
12. Han Y, Chun Q, Hua Y. Wind-induced vibration of traditional Chinese citygate buildings in the Ming-Qing dynasties-a case study of the Nanjing drum tower. Int J Archit Herit. 2023;17(4):615–34. doi:10.1080/15583058.2021.1953191.
13. Shi H, Jiang N, Zhou C, Zhnag Y, Yao Y, Zhou W, et al. Safety assessment of ancient Buddhist pagoda induced by underpass metro tunnel blasting vibration. Eng Fail Anal. 2023;145(7):107051. doi:10.1016/j.engfailanal.2023.107051.
14. Zhong Y, Li S, Jin W, Yan Z, Liu X, Li Y. Frequency domain analysis of alongwind response and study of wind loads for transmission tower subjected to downbursts. Buildings. 2022;12(2):148. doi:10.3390/buildings12020148.
15. Wei H, Cheng YJ, Peng ZY, Wang HJ. Finite element analysis for the wind resistance of the tower of wind turbine. Adv Mater Res. 2011;189–193:1718–21. doi:10.4028/www.scientific.net/amr.189-193.1718.
16. Wang J, Ning K, Tang L, Malekian R, Liang Y, Li Z. Modeling and finite element analysis of load-carrying performance of a wind turbine considering the influence of assembly factors. Appl Sci. 2017;7(3):298. doi:10.3390/app7030298.

17. Irwin PA. Wind engineering challenges of the new generation of super-tall buildings. J Wind Eng Ind Aerodyn. 2009;97(7–8):328–34. doi:10.1016/j.jweia.2009.05.001.
18. Janssen WD, Blocken B, van Wijhe HJ. CFD simulations of wind loads on a container ship: validation and impact of geometrical simplifications. J Wind Eng Ind Aerodyn. 2017;166(9–11):106–16. doi:10.1016/j.jweia.2017.03.015.
19. Prasad D, Uliate T, Ahmed MR. Wind loads on low-rise building models with different roof configurations. Inter J Fluid Mech Res. 2009;36(3):231–43. doi:10.1615/interjfluidmechres.v36.i3.30.
20. Jiang X, Yin Z, Cui H. Wind tunnel tests and numerical simulations of wind-induced snow drift in an open stadium and gymnasium. Adv Civ Eng. 2020;2020(1):8840759. doi:10.1155/2020/8840759.
21. Li X, He Q, Ling K, Wu H, Wang J, Liu D. Seismic response of masonry pagodas considering soil-structure-interaction (SSI) effect and CFRP reinforcement. npj Herit Sci. 2025;13(1):49. doi:10.1038/s40494-025-01580-7.
22. Zou D, Xu J, Cao Z. Simulation of fluctuating wind field and displacement response analysis of attached lifting scaffold. In: Proceedings of the Second International Conference on Advanced Manufacturing Technology and Manufacturing Systems (ICAMTMS 2023); 2023 May 26–28; Nanjing, China. p. 20–6. doi:10.1117/12.2688786.
23. Zhang XT. Wind resistant design and calculation handbook. Beijing, China: China Architecture & Building Press; 1998. (In Chinese).
24. Zhang XT. Structural wind engineering. Beijing, China: China Architecture & Building Press; 2006. (In Chinese).
25. Davenport AG. The spectrum of horizontal gustiness near the ground in high winds. QJR Meteor Soc. 1961;87(372):194–211. doi:10.1002/qj.49708737208.
26. Kaimal JC, Wyngaard JC, Izumi Y, Coté OR. Spectral characteristics of surface-layer turbulence. QJR Meteor Soc. 1972;98(417):563–89. doi:10.1002/qj.49709841707.
27. GB 50009-2012. Load code for the design of building structures. Beijing, China: China Academy of Building Research; 2012. (In Chinese).
28. Fang Z, Li C. Numerical simulation of instantaneous wind speed and wind load on cable-stayed cables. Vib Shock. 2010;29:210–2. doi:10.1016/b978-1-4832-8367-8.50127-3.
29. Luongo A, Zulli D. Parametric, external and self-excitation of a tower under turbulent wind flow. J Sound Vib. 2011;330(13):3057–69. doi:10.1016/j.jsv.2011.01.016.
30. Vijayan DS, Sivasuriyan A, Devarajan P, Stefańska A, Wodzyński Ł, Koda E. Carbon fibre-reinforced polymer (CFRP) composites in civil engineering application—a comprehensive review. Buildings. 2023;13(6):1509. doi:10.3390/buildings13061509.
31. Hegde S, Satish Shenoy B, Chethan KN. Review on carbon fiber reinforced polymer (CFRP) and their mechanical performance. Mater Today Proc. 2019;19(2):658–62. doi:10.1016/j.matpr.2019.07.749.
32. Benzeguir ZEA, El-Saikaly G, Chaallal O. Size effect in RC T-beams strengthened in shear with externally bonded CFRP sheets: experimental study. J Compos Constr. 2019;23(6):04019048. doi:10.1061/(asce)cc.1943-5614.0000975.
33. Haddad RH, Almomani OA. Flexural performance and failure modes of NSM CFRP-strengthened concrete beams: a parametric study. Int J Civ Eng. 2019;17(7):935–48. doi:10.1007/s40999-018-0342-8.
34. Van Cao V, Pham SQ. Comparison of CFRP and GFRP wraps on reducing seismic damage of deficient reinforced concrete structures. Int J Civ Eng. 2019;17(11):1667–81. doi:10.1007/s40999-019-00429-y.
35. Ozturk M, Sengun K, Arslan G. CFRP contribution to load-carrying capacity of retrofitted geopolymer concrete beams. Structures. 2023;48(7):1391–402. doi:10.1016/j.istruc.2023.01.028.